

Compressibility of hierarchic-architected agglomerates of hydrogen-reduced copper nanopowders

Dong-Hyun Ahn¹ · Wooyeol Kim¹ · Eun Yoo Yoon² · Hyoung Seop Kim¹

Received: 13 June 2015 / Accepted: 4 September 2015 / Published online: 15 September 2015
© Springer Science+Business Media New York 2015

Abstract Pure copper nanopowders are hydrogen-reduced in order to eliminate surface oxides and produce hierarchic architectures having inner-sponge structures with partially bonded nano/ultrafine particles and outer irregular-agglomerate boundaries. Due to a decrease in surface area by the particle bonding, the newly designed agglomerates exhibit improved surface stability after reduction, resulting in enhanced oxidation-resistance in the air at room temperature. For a comparative analysis, we also prepare two conventional micropowders having spherical and irregular particles. The compressibility of these three types of powders is analyzed using mechanical compaction. Finite element analyses on the compaction behaviors of the spherical and irregular particles are performed. The mechanical properties and microstructures of the compacts are investigated using microhardness tests, X-ray diffraction, and electron backscatter diffraction technique. Dislocation density, crystallite size, and grain size are correlated with the mechanical and compaction behaviors. From the analyses, three advantages of the

hydrogen-reduced copper nanopowder are noted: (1) suppression of oxidation while maintaining nano/ultrafine structure of particles, (2) lower pressure required for high-density compaction than for spherical powders with nano scale, and (3) favorable fabrication of bulk nano/ultrafine structures without cracks or fracture.

Introduction

Nano- and ultrafine-grained (NUFG) materials have attracted interest from many researchers and engineers for decades due to their unique properties (e.g., high strength, high fraction of grain boundaries, and high energy state of microstructure) [1–5]. Despite the interest, fabrication of bulk NUFG materials has remained a critical challenge to the researchers' efforts.

For manufacturing bulk NUFG materials, two approaches are generally used: top-down and bottom-up processes. Both approaches are actively employed for producing bulk NUFG materials. A top-down approach utilizes severe plastic deformation (SPD) to refine bulk materials' microstructure to nano/ultrafine scale. Typical examples include high-pressure torsion, equal-channel angular pressing, and accumulative roll-bonding processes [6–12]. Although the SPD processes can easily produce bulk NUFG structures, there exist some problems, such as limitation in minimum grain size, restrictions on the size and shape of bulk workpieces, and difficulty in microstructure control. Even though the bottom-up approach, by which bulk forms are produced from powders, has the potential to overcome the limitations in the top-down approach by controlling the properties of the initial powders, the process of consolidating particles to form bulk products also involves difficulty in achieving

✉ Hyoung Seop Kim
hyoungseopkim@gmail.com; hskim@postech.ac.kr

Dong-Hyun Ahn
dgkyunho@postech.ac.kr

Wooyeol Kim
prisious@postech.ac.kr

Eun Yoo Yoon
eyyoon@kims.re.kr

¹ Department of Materials Science and Engineering, POSTECH (Pohang University of Science and Technology), Pohang 790-784, Korea

² Commercialization Research Division, Korea Institute of Materials Science (KIMS), Changwon 641-831, Korea

bulk products of nearly full density, and maintaining the characteristics of the initial powders.

Two types of powders are generally used to create bulk NUFG materials: (1) micropowders with micro-sized particles and NUFG microstructures, and (2) nano/ultrafine powders having nano/ultrafine particle sizes [13–18]. For consolidation of micropowders with NUFG structures, conventional powder metallurgy works well. On the other hand, consolidation of the nano/ultrafine particles is generally more demanding due to their high surface to volume ratios, which cause strong oxidation and agglomeration. This makes nano/ultrafine particles unsuitable for fabricating bulk materials [19]. In order to minimize surface oxidation and particle agglomeration, the authors proposed a new approach that involves powders of microagglomerates of partially bonded nano/ultrafine particles produced using hydrogen reduction [9]. Using hydrogen-reduced NUFG copper powder, the quality of bulk product has been improved: higher strength, easier compaction, more solid bulk, etc. than without hydrogen-reduction [20].

Lee et al. reported the remarkable sintering property of the powders that are similar to the authors' hierarchic powders [21]. The hierarchic powder structure generates high-diffusion paths for densification during sintering processes, which provides strong potential for obtaining full-density bulk nanocrystalline solids. While the Lee et al. report that the hierarchic powders have good sintering characteristics, details of the compression behavior of powders with hierarchical architecture were not discussed.

In this study, powders with agglomerates of partially bonded nano/ultrafine particles were produced through hydrogen reduction of nano copper nanopowders. For further analysis on the morphology and size effect, micropowders with fine spherical and irregular particles were also prepared. The powders were mechanically compacted using a closed die in order to analyze their densification behavior and microstructural evolution. Moreover, finite element method (FEM) simulations of the powder compaction behavior were performed.

Experiment

Three types of copper powder were prepared: (1) hydrogen-reduced at 300 °C or 20 min with 3.5 °C/min heating rate to produce copper nanopowder having micro-sized agglomerates and inner nano/ultrafine (<1 μm) particles (hereafter, Hydrogen-Reduced NanoPowder: HRNP), (2) several μm sized copper micropowders with granular morphology (Spherical Powder: SPP), and (3) tens of μm sized and dendritic morphology (Irregular Powder: IRP). Scanning electron microscope (SEM) images of the three types are shown in Fig. 1.

Double-action quasi-static compaction in a die set of 10 mm diameter was implemented using an electro-mechanical testing machine (maximum load of 10 tons, Instron 1361, USA) and a hand-operated hydraulic compression tool (maximum load of 30 tons). Pressures up to 1 GPa were applied by the electro-mechanical machine and pressures >1 GPa were applied by the hydraulic compressor.

Cross sections of the compacted specimen parallel to the direction of compaction were polished with silicon carbide papers (400, 600, 800, and 1200 grit) and diamond suspensions (3 and 1 μm); then, the surfaces were etched with Nital etchant (nitric acid and diluted water, 50/50 %). The microstructure of the etched surface was observed using an optical microscope (OM, Olympus BX51M, Japan) and a field emission scanning electron microscope (FE-SEM, XL30S FEG PHILIPS).

For obtaining mechanical properties after compaction, microhardness tests were carried out at room temperature using a Vickers hardness tester (FM-700, Future-Tech. Co., Japan) with 300 g and 10 s, load and dwell-time, respectively.

The X-ray diffraction (XRD) patterns of the compacted specimens were acquired using an X-ray diffractometer (D/Max-2500/PC, Rigaku, Japan); then, the peaks of these patterns were analyzed using the convolutional multiple whole profile (CMWP) method [22] to obtain their microstructural information.

An electron backscatter diffraction (EBSD) technique was conducted on the cross section surfaces in order to examine their specific microstructure, including geometrically necessary dislocation (GND) density (calculated based on Nye's theory) of the compacted specimens [23]. Before observations, the surfaces were mechanically polished up to 1 μm diamond suspension and then electrochemically prepared using an electric polisher (LectroPol-5, STRUERS) with an etchant (D2 solution) at 24 V and room temperature.

Simulation

Explicit FEM simulations using the commercial software Abaqus 6.9EF were performed for the compaction process of two types of powder: the irregular- and spherical-shaped particles. The morphologies of these two powders were modeled based on the SEM images of HRNP and SPP, as shown in Fig. 2a, b. Figure 2c is the irregular particle model imitating Fig. 2a. In addition, spherical particles (Fig. 2d) were modeled by random generation in an effort to imitate the particles in Fig. 2b. The relative density of spherical model is similar to that of the irregular model shown in Fig. 2c, d.

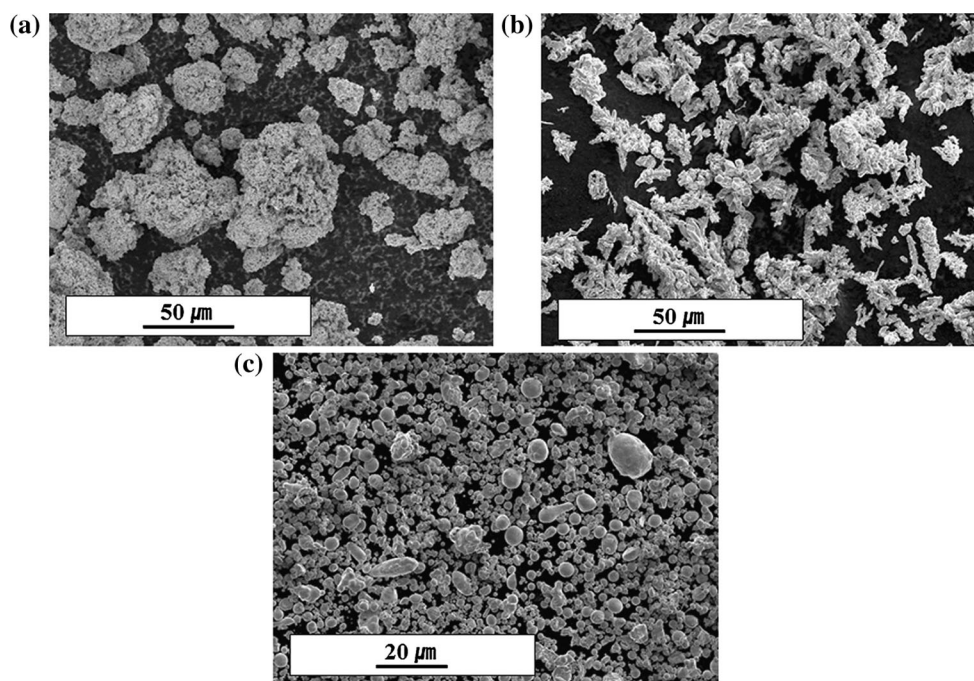
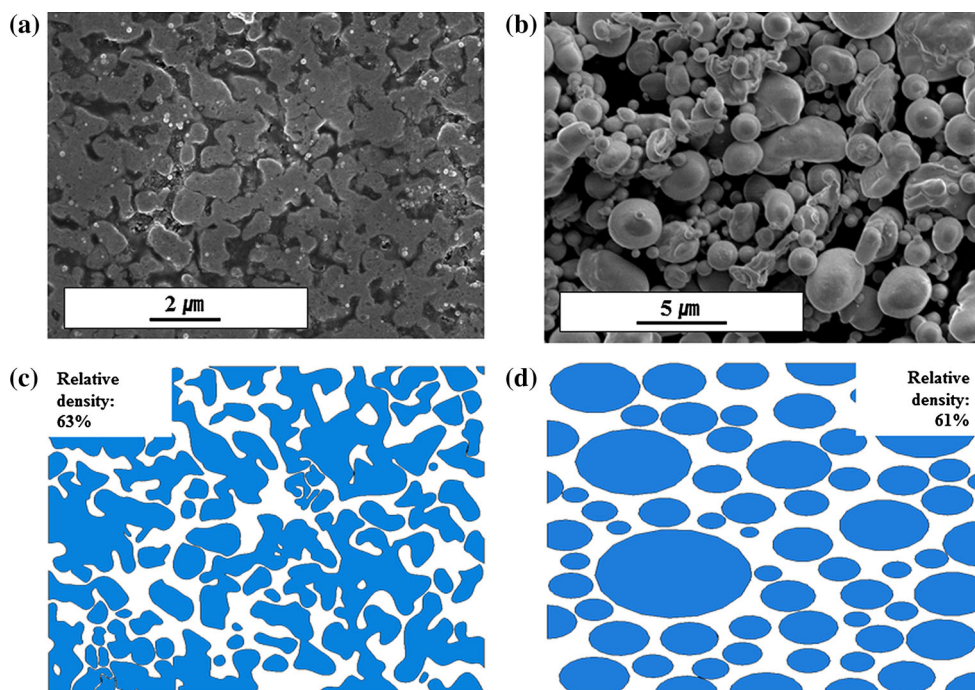


Fig. 1 Scanning electron microscope images of the **a** hydrogen-reduced copper nanopowders (HRNP), **b** irregular powders (IRP), and **c** spherical powders (SPP)

Fig. 2 SEM images of **a** HRNP and **b** SPP. Powder models **c** and **d** for FEM simulations of IRP and SPP compactions from the images **a** and **b**, respectively



For simplicity, a 2-dimensional plane-strain condition was selected with $12.47 \times 9.45 \mu\text{m}^2$ sized rigid compaction box. The compaction process was controlled using the displacement boundary condition. In the basic simulation, 0.1 was chosen as the friction coefficient; in addition, the mechanical properties of commercial copper solid were

used: 110 GPa, 0.36, 150 MPa, and 350 MPa as Young's modulus, Poisson's ratio, yield stress, and saturated stress, respectively. In order to analyze the effects of friction and the mechanical properties, frictionless conditions between particles and the harder materials than the basic simulation were also applied.

Results

Relative densities (RDs) were evaluated using the dimensions of the compacts and their mass based on the full solid density of copper 8.93 g/cm^3 . Figure 3 presents the compaction curves of the three types of copper powders. The SPP had a higher initial RD than did the other two powders, IRP and HRNP. However, IRP and SPP showed very similar compaction trends after $\sim 75.0\%$ RD. After the cross point between the compaction curves of IRP and SPP, the required pressure of IRP was lower than that of SPP. The HRNP showed a similar trend as IRP throughout the entire compaction process, except for a difference in RDs at the same pressure.

Figure 4 exhibits the optical microscopic images of the cross section of the three compacts. It was found that particle boundaries were more etched than the other regions, meaning that etched lines depict particle shapes, not grain morphologies. In the cross section of the SPP compact (Fig. 4a), the etched microstructure shows the deformed spherical morphologies originated from the initial spherical particle. However, it was not possible to figure out the initial particle shape from the deformed particle shape in the IRP case (Fig. 4b). HRNP (Fig. 4c) showed much finer particle boundaries than the others (IRP and SPP). Such fine microstructures are primarily due to inner nano/ultrafine particles.

Figure 5 presents the SEM images of the compacts. The particles of SPP had a polyhedron-like shape due to the initial particle morphology. This spherical shape makes it difficult to produce strong particle interlocking leading to particle detachments, as shown in Fig. 5a (marked by circles of dots). The particles of IRP (Fig. 5b) exhibited no such detachment. Initially connected particles due to the morphology of IRP and deformations caused by bending

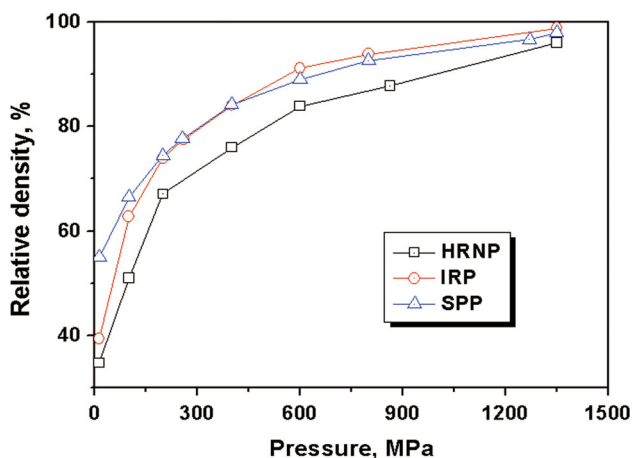


Fig. 3 Pressure versus relative density curves of the HRNP, IRP, and SPP

the connections (marked with a red-dotted arrow), are observable. In the microstructure of SPP and IRP, the apparent particle size for IRP was larger than that of SPP. From the HRNP image, it is clear that the particle size of HRNP was finer than for the other two powders, and that the particles were connected by particle-bridges as in the case of IRP (such bridges are directly confirmed in Fig. 2a).

The simulated compaction process of irregular particles is presented with equivalent plastic strain contours in Fig. 6. Each contour shows the states at RDs of 69.0, 79.0, 89.0, 97.0, 99.7 %, and apparent full density (100.0 %). RDs were evaluated using the lengths of the compacted region and the initial mass. Deformations started with intense strains at local bridge regions. As pressure and RD increased, inter-particle contact regions also increased. Plastic strains were lower than 1.0 in most regions, and the particles' surface and some bridge regions that could be bent during deformation underwent larger plastic strain than the other regions. Due to differences in particle size, some small particles underwent overall deformation. On the other hand, relatively less strain was generated in the center region of the large particles.

Similar equivalent plastic strain contours of the spherical particles during simulated compaction are also shown in Fig. 7. Plastic deformation started at the contact surfaces of the particles. Similar to the irregular case, some small particles located around large particles were more deformed than the others. Compared with the simulation of irregular particles, spherical particles did not show any bending deformation.

Both types of particles did not exhibit perfect closure of voids at the theoretical volume for full solid copper density (from the mass of the particles and the dimensions of the box in the simulation). Further compaction (or over compaction) was required to close all the voids to reach apparent full density in the simulation (as shown in Figs. 6, 7). This over compaction phenomenon could be attributed to elastic compression of the particles, by which the volumes of particles are decreased. This elastic compression was achieved by pressure generated by frictional and geometric effects during the deformation flow of particles into voids, like barreling phenomenon in compression of cylinders. For example, when compressing cylinders having frictional interfaces, heterogeneous deformation due to the curved side generates inner pressure, which increases the work needed to compress the deforming cylinder.

Pressures during compaction were calculated using the area of compaction die used in the simulation, and the reaction force applied to the surface. This evolution of pressure during compaction was extracted and the densification curves are shown in Fig. 8. For the irregular particles, RD continuously increased from 63.0 to almost

Fig. 4 Optical microscope images on the cross sections of the **a** SPP, **b** IRP, and **c** HRNP after the compactions

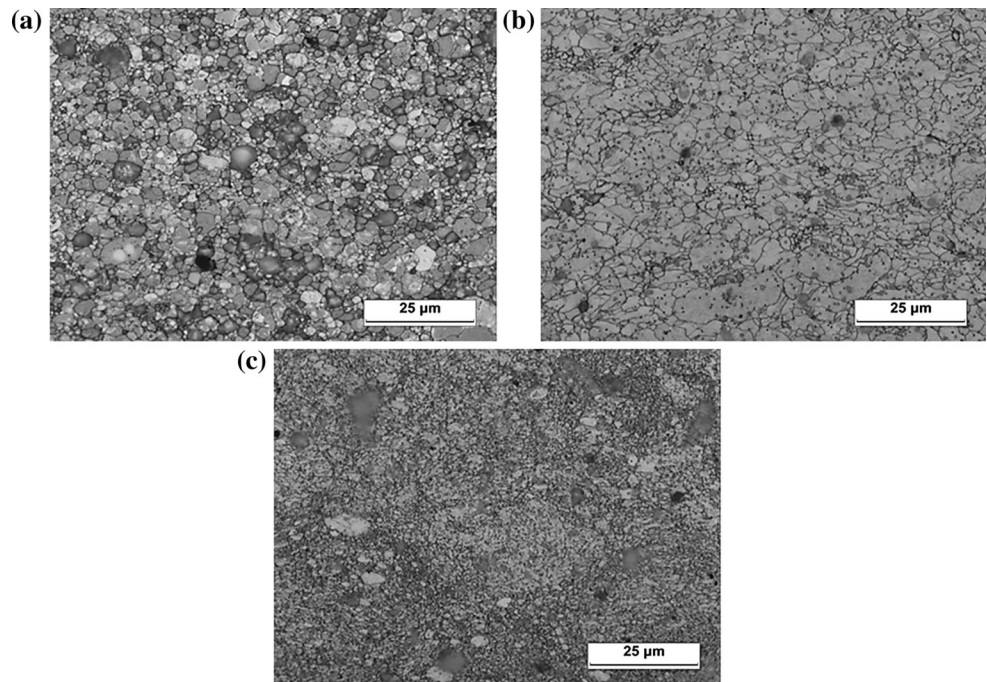
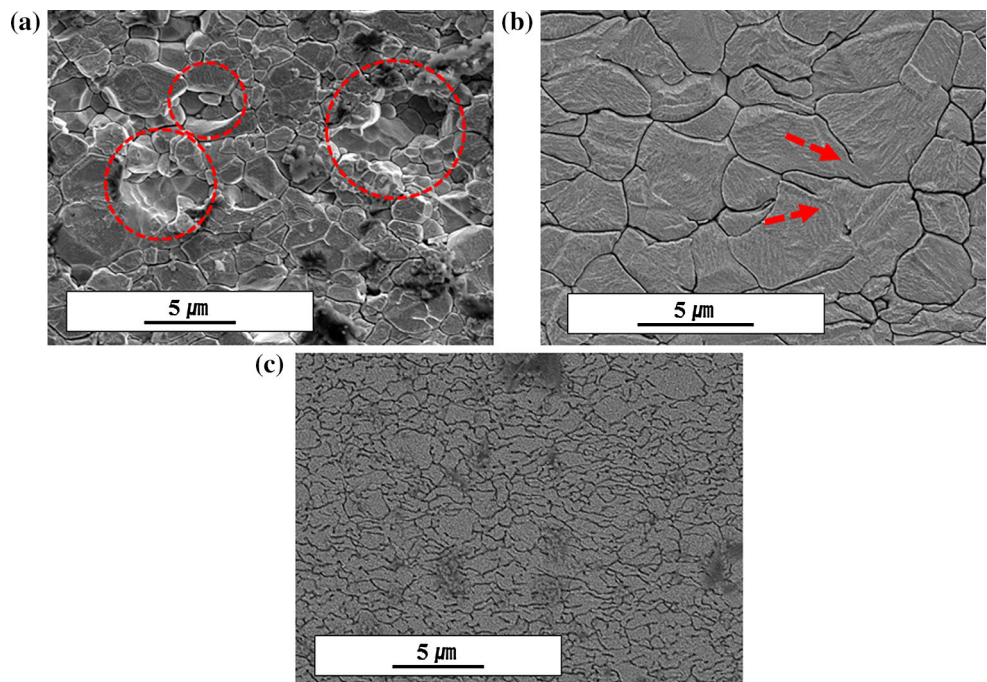


Fig. 5 SEM images on the cross sections of the **a** SPP, **b** IRP, and **c** HRNP after the compactions



100.0 %. Because some regions were first deformed locally in the powder structure with complicated connections, stress lower than the yield stress (shown as lines in Fig. 8) was needed until 88.0 % RD. After this point, the pressure required increased steeply due to a combination of conditions: increase of deforming regions, hardening of particles, and frictions between particles. At about 96.0 % RD, the stress required for further compaction exceeded the

maximum stress of the powders because of the geometric and elastic deformation effects for filling the small voids.

For further understanding, simulations using a frictionless condition and another simulation using stronger mechanical properties that represent powder having smaller particles were performed and the resulting compaction curves are shown in Fig. 8. From the frictionless case, it is found that friction increases the required pressure slightly,

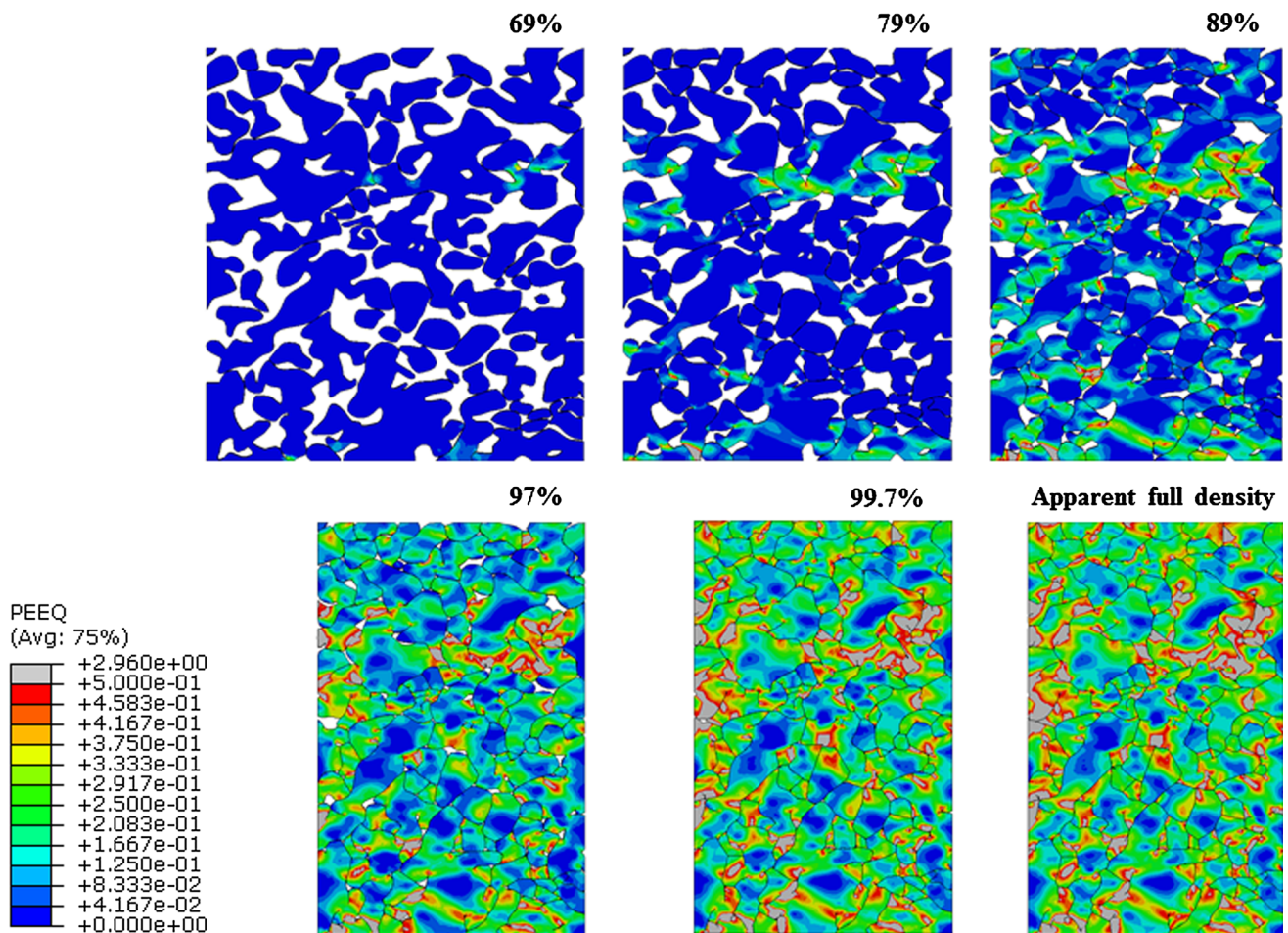


Fig. 6 Equivalent plastic strain distributions during compaction at 69.0, 79.0, 89.0, 97.0, and 99.7 % RD, and apparent full density in the FEM simulation of the irregular powders (IRP)

but does not change the compaction trend. Harder particles moved the compaction curve upward and steepened the slope. The RD achieved at yield stress of the harder particles was higher than the RD of the softer particles at the yield stress of the softer particles; however, in both cases, the maximum stresses reached about 96.0 % of full density.

The spherical particles presented a different trend in the compaction curve. The pressure increment started at about 80.0 % RD; then, the pressure increased steeper than in the case of irregular particles. The pressures required for the irregular and the spherical particles crossed over at about 88.0 % RD. The basic simulation models were carried out with identical mechanical properties and simulation conditions; therefore, it could be concluded that the differences in the compaction curves result from differences in particle morphology.

In summary, the results of the simulation including densification curves of irregular and spherical particles,

and irregular particle with harder properties give the following insights for analyzing IRP, SP, and HRNP: (1) IRP shows initially lower RD than SP, then after the critical RD, inversion of RDs between IRP and SP occurs due to difference in morphology. (2) The reason for higher required pressure of HRNP is mainly the smaller particle size accompanying stronger mechanical properties. (3) RD below 100 % after the maximum stress of particle is attributed to geometric and elastic deformation effects.

Microhardness values after the compactions at 1.35 GPa pressure (98.9, 98.0, and 96.0 % RDs for IRP, SPP, and HRNP, respectively) are shown in Fig. 9. SPP and IRP, having relatively coarse sizes but differently shaped particles, showed very similar hardness values at about 130 Hv, whereas HRNP with nano/ultrafine particles was about 150 Hv. The hardness in HRNP was comparable to that in severely plastic deformed pure copper [24].

After the compactions, dislocation densities and crystallite sizes from the XRD patterns were analyzed and are displayed

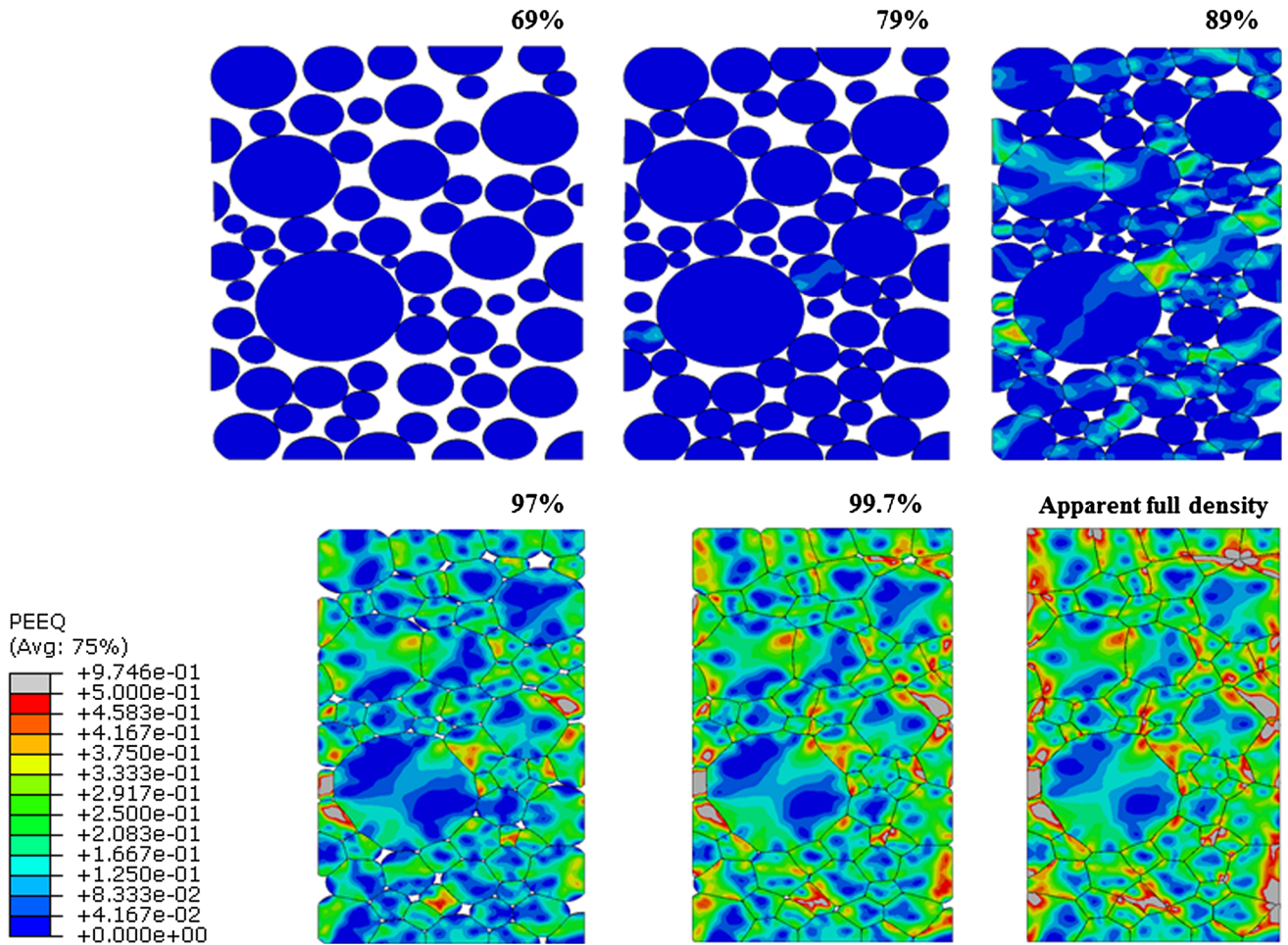


Fig. 7 Equivalent plastic strain distributions during compaction at 69.0, 79.0, 89.0, 97.0, and 99.7 % of RD, and apparent full density in the FEM simulation of SPP

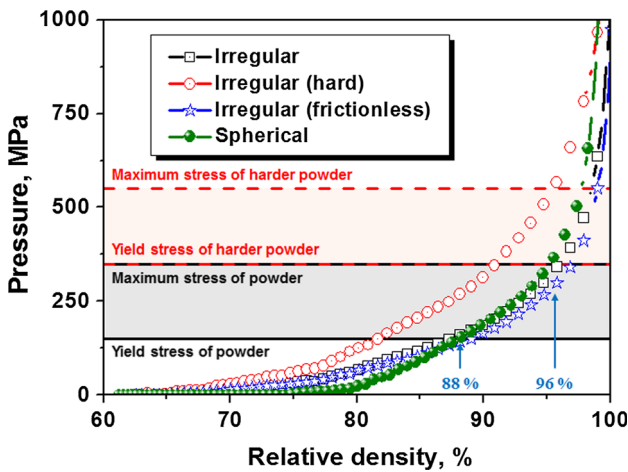


Fig. 8 Calculated pressure versus relative density of the irregular (basic, harder, and frictionless conditions) and spherical powders

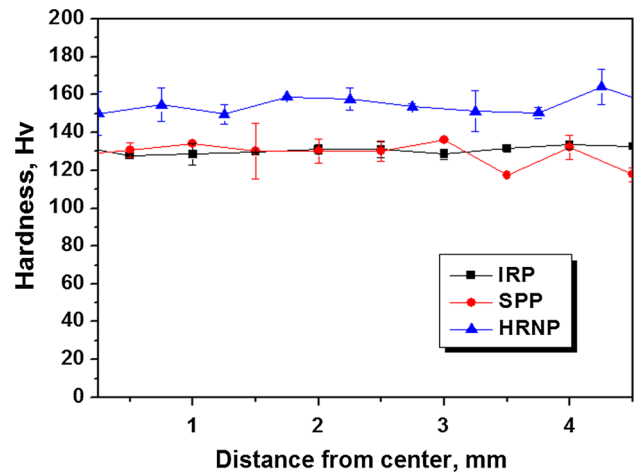


Fig. 9 Microhardness distributions from the center to the edge on the cross section of the cylindrical compaction sample

in Fig. 10. The measured dislocation densities and crystallite sizes were 3.0×10^{15} , 4.0×10^{15} , $8.7 \times 10^{15} \text{ m}^{-2}$; and 104, 111, 76 nm; for IRP, SPP, and HRNP, respectively.

The information about microstructure from inverse pole figure (IPF) maps is shown in Fig. 11. Low confidence index region data were shown in black. Such regions of

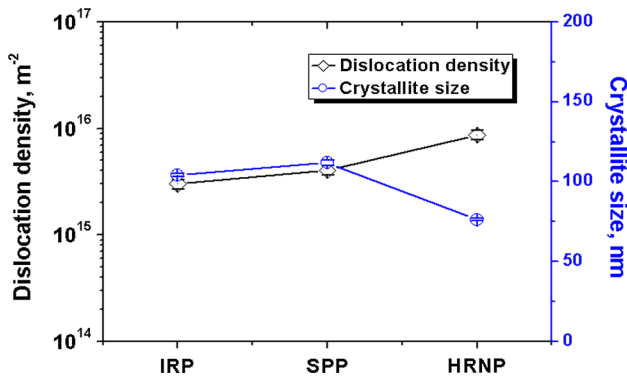


Fig. 10 Dislocation densities and crystallite sizes of IRP, SPP, and HRNP after compactions, evaluated using the XRD line profile analysis

data loss could come from largely deformed regions and particle boundaries having deeper etch pits than the interiors of the particles did. The compacts of the IRP and SPP had qualitatively similar microstructures; however, HRNP showed distinctly smaller grain size and more lost points due to the large area of particle boundaries than others. From the IRP and SPP maps, it was concluded that each particle included several grains; on the other hand, the particles in HRNP normally have one grain per particle.

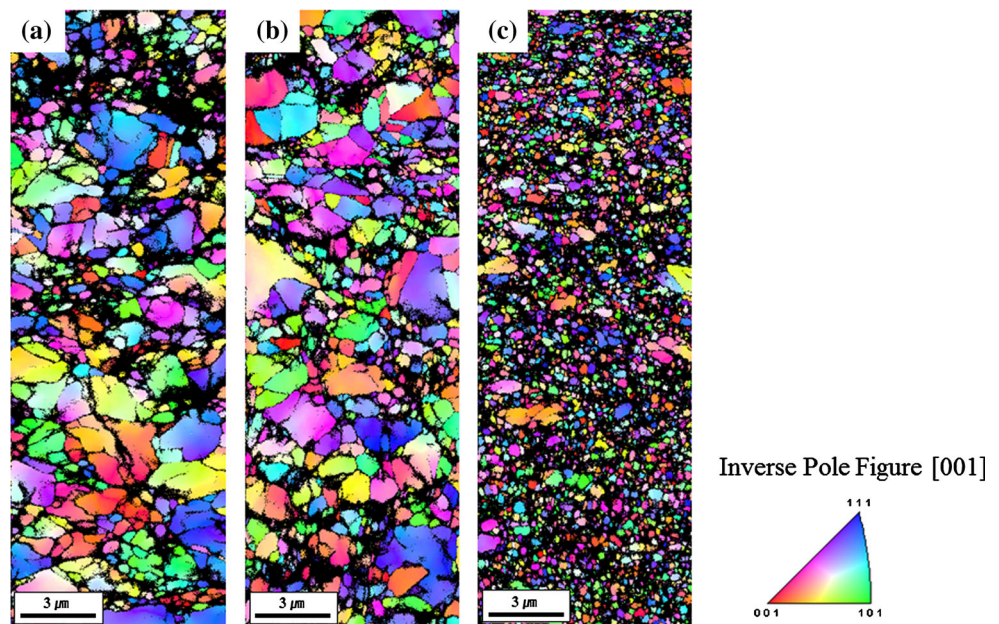
Figure 12 shows the grain size distributions of the three compacts from the EBSD results and the average grain sizes at the top of each distribution. Similar to the qualitative results of the IPF maps, the grain size distributions and average sizes (1.2 and 1.1 μm), of the IRP and SPP

shown in Fig. 12a, b, were quantitatively very similar. The HRNP distribution (shown in Fig. 12c) shows very small grain size (~ 300 nm) and an average of roughly 360 nm.

Deformation distributions represented as kernel average misorientation (KAM) maps in the EBSD results are shown in Fig. 13. For comparison, image quality (IQ) maps outlining particles are also displayed in the figure. For IRP (Fig. 13a), some particles had highly deformed interiors showing low IQ values. The particles having highly deformed interiors are marked by dotted red circles in the IQ image of the IRP compact. On the other hand, it is difficult to find highly deformed regions in the particle interiors of SPP. This difference could be caused by the morphologies of the particles. The simple spherical particles have undergone intensive plastic deformation at particle boundaries due to their shape, while particles with complicated morphology, like IRP, generally have highly deformed regions not only at the particle boundaries but also in some inner regions, where bending or intense deformation at the connection between particles occurs. This different deformation trend is also found in the FEM simulations, in Figs. 6 and 7. Particles of HRNP having the similar morphology to those of IRP also showed highly deformed interior regions (small circles of red dots as an example). Moreover, larger particle boundaries of HRNP than ISP and SPP led to more homogeneous distributions of the highly deformed area (over ~ 1 of KAM).

Based on the EBSD maps, geometrically necessary dislocation (GND) densities were evaluated and are shown in Fig. 14. Qualitatively, regions, near particle boundaries

Fig. 11 Inverse pole figure maps from electron backscatter diffraction (EBSD) on the cross sections of the a IRP, b SPP, and c HRNP



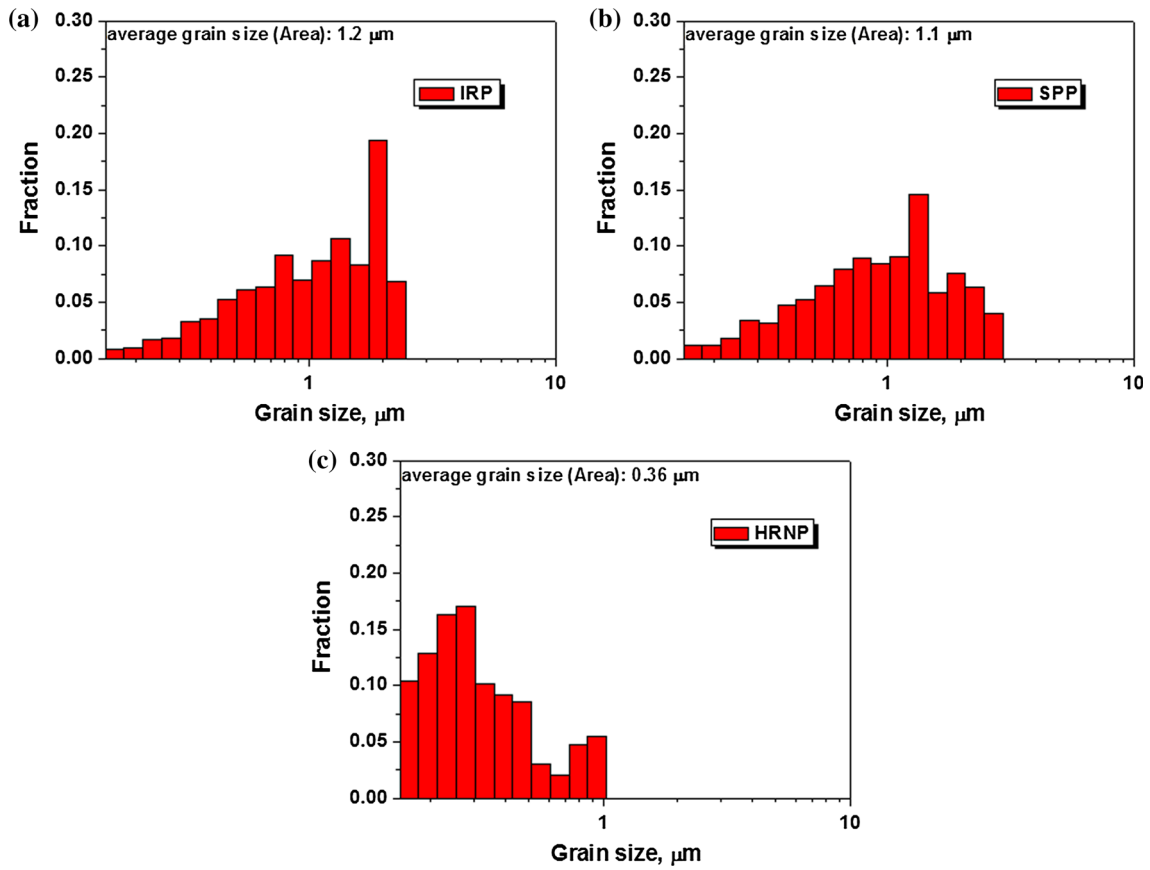


Fig. 12 Grain size distributions and area averaged grain sizes of the **a** IRP, **b** SPP, and **c** HRNP from the EBSD results

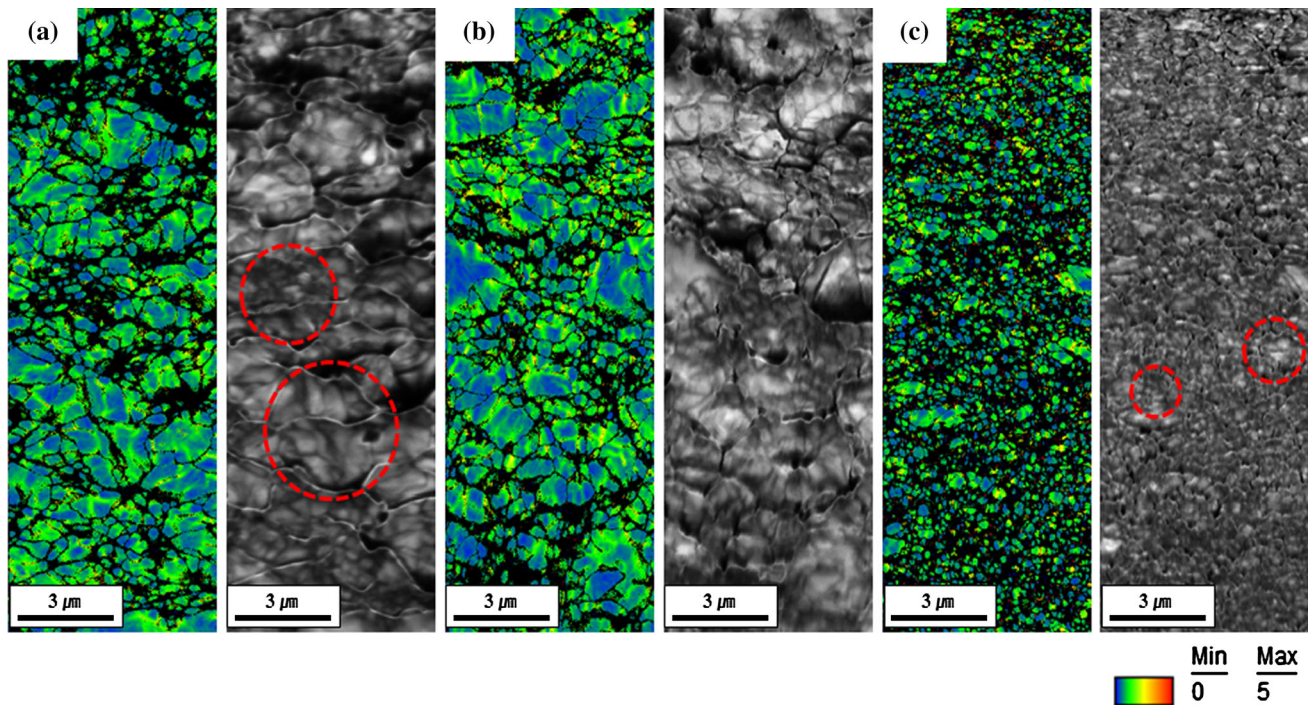
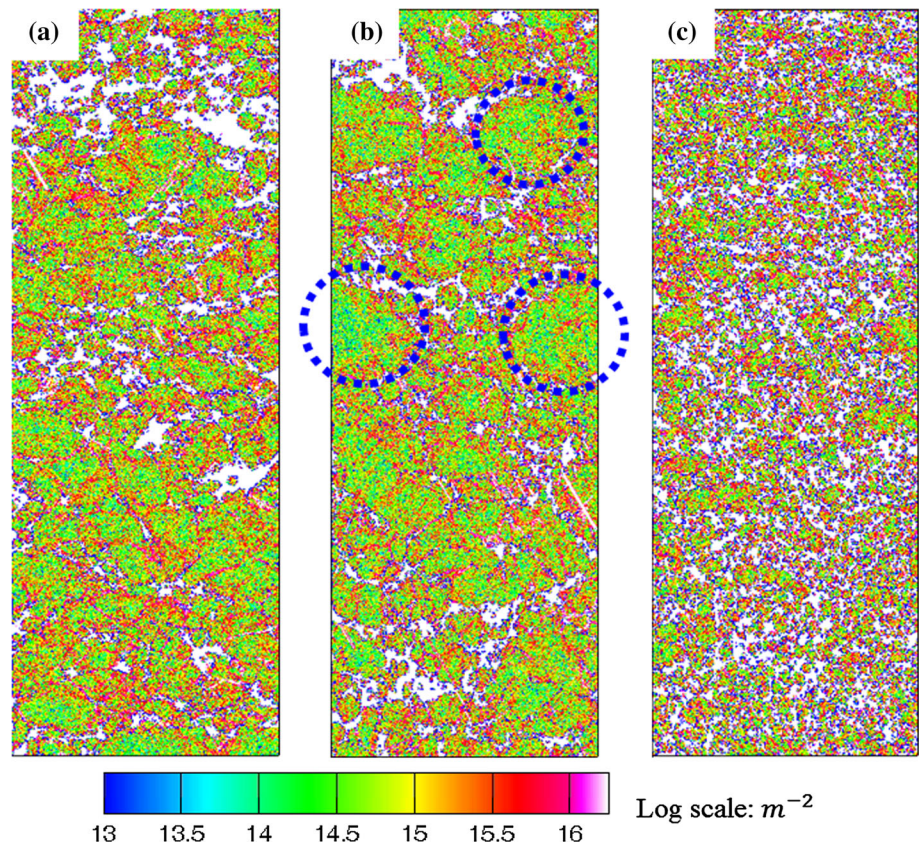


Fig. 13 Kernel average misorientation (KAM) and image quality (IQ) maps of the **a** IRP, **b** SPP, and **c** HRNP from the EBSD results

Fig. 14 Geometrical necessary dislocation (GND) density (log scale) distributions of the **a** IRP, **b** SPP, and **c** HRNP



or grain boundaries, had higher GND densities than the interior of particles or grains. These distributions of GND are similar to the strain distribution in the FEM simulation and the distribution of misorientation in the KAM maps. Between IRP and SPP (Fig. 14a, b), no clear difference was found except that some particles (marked with blue dotted circles in Fig. 14b) had depleted GND densities. According to the FEM simulation of SPP, the spherical geometry of SPP gives rise to these depleted regions in the interiors of the particle. Compared to SPP, the IRP particles scarcely show the depleted GND density regions. Instead, narrow regions of high GND density ($\sim 10^{15} \text{ m}^{-2}$) are more frequently found in IRP than SPP due to bending or geometrical flow deformation of irregularly shaped particle. Although HRNP exhibited a morphology similar to that of IRP, the smaller particle size and consequentially larger grain boundaries of HRNP generated significantly higher GND density distribution than for the others.

For a more detailed comparison, quantitative data extracted from the GND contours are demonstrated in Fig. 15. It could be noted in Fig. 15a that the GND distributions of IRP and SPP had very similar trends, while HRNP had a higher fraction of high GND density regions. The average and median values of the distributions are summarized in Fig. 15b. Although the distributions of IRP

and SPP were very similar, the average and median values were slightly higher in the SPP. Compared to the microcompacts (IRP and SPP), the HRNP had distinctly higher values. This relative difference in GND densities among compacts was also found in the total dislocation density measured via the XRD line profile analysis (Fig. 10).

Discussion

The effect of particle morphology

Before compaction, powders of irregularly shaped particles generally have lower apparent RD than do spherical particles [25]. Both IRP and HRNP had irregular shapes (dendritic, and sponge-like with irregular boundaries, respectively; see Fig. 1a, b). The effect of the irregular particle shapes on the compaction is shown in Fig. 3. The RDs of IRP and HRNP at ~ 10 MPa of applied pressure were below 40.0 %; on the other hand, the SPP had an RD of ~ 55.0 %. This difference between IRP and SPP started to disappear as compression progresses; then, the trends of compaction became similar after ~ 75.0 % RD at 200 MPa. This curve matching indicates that the effect of the irregular particle shape on the compaction of the

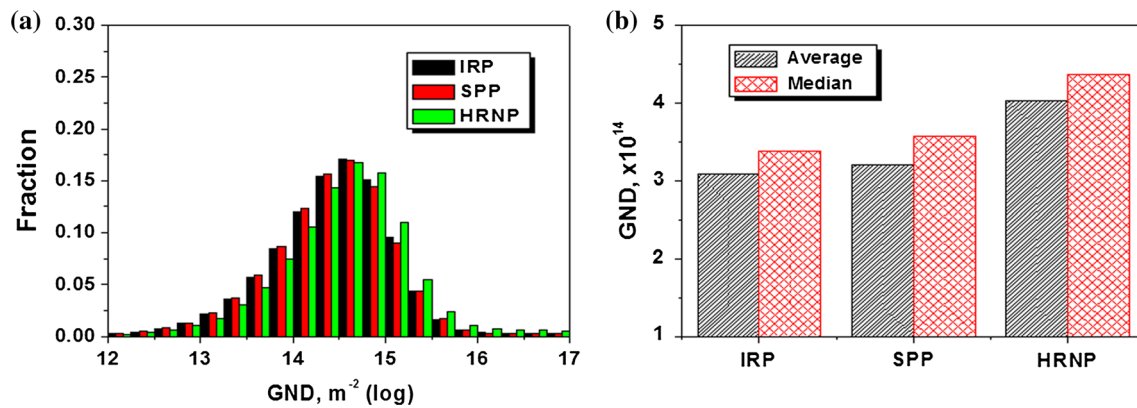


Fig. 15 Quantitative analysis results from the GND (m^{-2}) calculation: **a** distributions of the density fraction and **b** average and median values of the distributions of log GND densities of the IRP, SPP, and HRNP

powders is dominant in the early stage and becomes minor after a critical RD, as was evident in the simulation results.

The behavior of IRP and SPP after the curve matching was similar, except that SPP required slightly higher pressure to achieve the same RD. According to the microhardness results in Fig. 9 and the grain size in Fig. 12, the IRP and SPP compacts, with similar initial grain sizes, had the similar final and initial mechanical properties since no refinement in grains having high-angle grain boundaries can occur during compaction. This indicates that IRP and SPP particles had comparable mechanical properties during the compaction processes. The phenomenon that spherical particles require a higher pressure than irregular particles to reach the same RD, even though the particles have the same mechanical properties, was also observed in the simulation curves (Fig. 8). This difference in the required pressures caused by the powder morphology means that irregular particles could be compacted using less pressure than for spherical particles at high RD.

HRNP also showed the feature of irregular particle shapes, low initial density, and a slow increase in required pressure in the compaction curve (Fig. 3). In HRNP, not only irregular shapes of agglomerates but also sponge-like forms of powders contribute to the features of irregular particles. Both the irregular shapes and the sponge forms of HRNP have negative effects on packing particles, which indicates particles will be less densely packed. Moreover, these negative features work concurrently in the early stage of compaction. Therefore, HRNP has the strong tendency to having a larger volume per mass than IRP does. As a result, at 10 MPa, a lower RD is obtained for HRNP than for IRP. Kim et al. proposed a densification model of agglomerated particles adaptable to HRNP [26]. In the model, two phases in an agglomerate (interior with sponge form and irregular boundary phase) were proposed. Irregular particles of HRNP could be considered as agglomerate

having connections between constituent particles. According to the model, the agglomerate boundary phases are densified first, until the RD of the boundary phases equals the RD of the agglomerate interior phase. After that, the densification behaviors of the two phases are predicted to be the same. The two-phase model demonstrates why HRNP has the lowest RD and a stronger irregularity effect than IRP, despite their similar particle morphology, and how this effect disappears during compaction.

Microstructural evolution

During compaction, the particles underwent large plastic deformation under high pressure. It is hard to experimentally measure the deformation strains of the individual particles; on the other hand, their equivalent strain could be quantitatively evaluated using FEM, as shown in Figs. 6 and 7. Average strains within IRP and SPP, calculated by considering non-uniform sizes of the elements, $\varepsilon_{\text{average}} = (\sum V_{\text{element}} \varepsilon_{\text{volume}}) / \sum V_{\text{element}}$, are ~ 0.260 and ~ 0.216 , respectively. Irregular particles are deformed more than spherical particles due to local bending deformations during compression. Larger plastic deformations generally indicate more dislocations generated; however, the evaluated dislocation densities from the XRD line profile analysis in Fig. 10 show results contrary to the simulations. That is, IRP was expected to have higher dislocation density due to relatively larger deformation.

This inconsistency resulted from the particle size effect. It should be noted that relative size difference between irregular and spherical particles used in the FEM simulations is not the same, compared to that between IRP and SPP. As seen in the OM and SEM images of Figs. 4 and 5, SPP had smaller particles than IRP; however, spherical particles of the FEM simulations had a relatively large size. As a result, it could be concluded that the area of deformed particle surfaces is larger in SPP particles than those used

in the simulation. Therefore, the effects of morphology in dislocation evolution canceled out and relatively higher dislocation density in the SPP was obtained due to the size effect.

Microstructure refinement with high-angle grain boundaries was not achieved in all three compacts due to the low strain (i.e., strain <1) [7]. In the EBSD image (Fig. 11), only deformed grains without noticeable refinement were found. The area of deformation in the Kernel average misorientation (KAM) distribution (Fig. 13) can be compared with the FEM simulation. The IRP particles had homogeneously deformed regions due to compression and bending deformations, and the simulation also showed such homogeneous deformation. The SPP also showed a trend similar to that in the simulation, where the particle surfaces had larger strains than the inner regions. A peculiarity in the experimental results is that KAM values are also intense near the grain boundaries, which act as a barrier of dislocation movement in crystal plasticity, and this feature was not included in the simulation. However, since the grain sizes of IRP and SPP were almost the same, it is reasonable that this grain boundary effect could be excluded for analysis of the dislocation densities of IPR and SPP.

That HRNP has smaller particle size and more irregular morphology than the others, indicates that large deformation was applied. The large deformation of HRNP leads to higher dislocation density than observed in the others, as shown in Fig. 10. In addition, according to the comparison results between IRP and SPP, it is expected that HRNP should have higher and more homogeneous dislocation density distribution than would spherical particles at a similar nano/ultrafine scale with HRNP.

The GND result in Fig. 15 also demonstrates the high dislocation density of HRNP caused by small particle size and large surface area. In the distribution shown in Fig. 15a, the center of distribution of HRNP moves toward greater density than the other powders. As seen in both the FEM simulation and the EBSD result, the particle surfaces with severe deformation had much dislocations generated than did the inner region of particles. Consequently, the fraction of high GND density increased in HRNP. This trend of GND densities from the EBSD result shows a good agreement with the total dislocation densities measured using XRD.

Mechanical property

There are two major aspects of the mechanical properties of compacts that should be considered: the strength of the final compact, and the effect of mechanical properties of the initial powder on the compaction process. The former relating to the final microstructure is important for handling the compact without catastrophic fracture. The latter

significantly affects the process of synthesizing bulk materials.

There are also four factors related to the mechanical properties of the final compacts to consider: dislocation density, grain size, porosity, and particle interlocking. The two microstructural features, dislocation density and grain size, represent intrinsic mechanical and microstructural factors regardless of the state of bonding among particles. The other two factors, porosity and particle interlocking, are related to the geometry of compacted particles. The microhardness ($\sigma_{\text{microhardness}}$), which has a compressive nature, is a function of dislocation density, grain size, and porosity, and can be expressed as follows:

$$\sigma_{\text{microhardness}} = f(\sigma_{\text{dis}}, \sigma_{\text{gs}}, p), \quad (1)$$

where σ_{dis} , σ_{gs} , and p are the stress contributed by dislocations, the stress induced by the grain size effect, and the porosity of the compact, respectively. The strength σ as a function of porosity can be expressed as follows [27]:

$$\sigma = \sigma_0 \left(1 - 1.19p^{2/3}\right), \quad (2)$$

where σ_0 is the strength of a full density material. Using this equation with the average hardness and the RD of the three experimental compacts, calibrated hardness can be determined: 139.24 Hv for IRP, 141.09 Hv for SPP, and 179.26 Hv for HRNP. The flow stress could be obtained by multiplying these hardness values by 3.3: 459.5 MPa for IRP, 465.6 MPa for SPP, and 591.6 MPa for HRNP, respectively. It should be noted that the flow stresses calculated by multiplying 3.3 to hardness are compressive strengths not tensile strengths. Because defects in tensile deformation can decrease the apparent strength of a material, the conversion factor 3.3 between tensile strength and hardness may not be valid in some brittle materials [28]. On the other hand, compressive strength exhibits good correlation with hardness using the conversion factor 3.3 even in case a material exhibits brittle tensile fracture [20].

Grain size and dislocation density are generally related to mechanical properties by the conventional Hall–Petch (H–P) relation and Taylor expression:

$$\sigma = \sigma_f + k_1 d^{-1/2} \text{ (Hall–Petch relation)}, \quad (3)$$

$$\sigma = \sigma_f + \alpha M G b \sqrt{\rho} \text{ (Taylor relation)}, \quad (4)$$

where σ_f , k_1 , and α are constants, and d , M , G , b , and ρ are the grain size, the Taylor factor, the shear modulus, burgers vector, and dislocation density, respectively. Generally, the trends of dislocation density and (grain size)⁻¹ with plastic strain during plastic deformation are the same. Therefore, either the H–P relation or the Taylor relation can explain the mechanical behavior of metallic materials, if grain size or dislocation density, respectively, can be measured [29,

30]. The relation type and the parameters should be chosen depending on the state of a material. Equations (3) and (4) can be used when a measurable microstructural factor is grain or substructure boundaries, or dislocation densities, respectively [31]. In the three experimental compacts, three models can be considered: (1) H–P relation and the grain size from EBSD, (2) H–P relation and crystallite size from the XRD line profile analysis, and (3) Taylor relation and dislocation density from the XRD line profile analysis.

In the first model (H–P relation and grain size from EBSD), the evaluated flow stresses σ with 20 MPa of σ_f and 0.149 MPa m^{1/2} of k_1 are 156.25, 162.31, and 268.77 MPa, for IRP, SPP, and HRNP, respectively [32]. In the second model (H–P relation and crystallite size from XRD), the calculated flow stresses for IRP, SPP, and HRNP are 492, 470.03, and 561.42 MPa, respectively. In the last model (Taylor relation and dislocation density from XRD), the obtained flow stresses for IRP, SPP, and HRNP (using 0.198 of α [33], 0.256 nm of b , 3 of M , and 45 GPa of G) are 387, 445, and 649 MPa, respectively. Compared to the experimental results, the second model shows very good agreement. Although the H–P relation and crystallite size from the XRD line profile analysis quantitatively well predict the strength of the compacts, it does not demonstrate that dislocation density is not a governing factor of strength. This analysis indicates that the mechanical property of the compacts is mainly governed not only by high-angle grain boundary but also by crystallite boundaries acting as barriers to dislocation motions.

Despite the excellent compressive properties, the tensile properties of these materials are relatively poor due to the weak bonding between powders (i.e., there is only mechanical bonding between particles). Although mechanical bonding, like interlocking of particles, is not enough to sustain tensile plastic deformation, the bonding is strong enough to handle the final compact without fracture. In this context, particles of irregular morphology are superior to spherical particles. For example, the SPP compact showed cracks, fractures, and even detachment of particles, as shown in Fig. 5, despite that its mechanical properties, microstructural features, and compaction behavior were similar to those of IRP compact. The morphology effect on mechanical bonding means that irregular particles are advantageous for creating bulk compacts.

By the simulations and experiments on the compaction of the three different types of powder, the mechanical and microstructural properties of the compacts were assessed. The HRNP material shows the following benefits. (1) The formation of agglomerate in HRNP having connections of nano/ultrafine particles suppresses oxidation that is an obstacle for compaction of conventional nano/ultrafine powders. (2) Even though lower RD is predicted for HRNP than for the spherical

nano powders with similar mechanical properties at the beginning of the compaction, higher RD could be acquired under the same pressure after the critical cross point. (3) Bulk materials of high strength, caused by NUFG microstructure and high dislocation density, could be fabricated from HRNP. Moreover, the compact could be handled and processed without cracks or fractures due to its irregular morphology.

Conclusions

In this study, newly designed powders subjected to hydrogen reduction have been analyzed via simulation and experiment. The analyses cover the morphology of particles as well as the properties of the final compacts. The following conclusions were drawn.

- (1) A hierarchic structure consisting of outer micro-sized irregular agglomerates, and inner nano/ultra-fine irregular particles was developed. The HRNP powders with the hierarchic structure have relatively stable surfaces resistant to formation of oxidation layers. Hence, the effect of oxidation on the compaction process was eliminated within HRNP. This elimination of oxidation makes high RD possible through mechanical densification. Therefore, a bulk material is easily fabricated from HRNP.
- (2) Irregular particles show lower RD at the beginning of compaction than that of spherical particles in both the experimental and simulated results. However, the trend of the compaction is reversed after a critical point, after which irregularly shaped particles require less pressure to achieve the same RD. This lower required pressure indicates that HRNP is advantageous in fabricating high RD compact; moreover, the irregular particles exhibit stronger interlocking than do spherical particles, which enables control of compacted bulk without cracks or fractures.
- (3) From the results of the experiments and simulations, microstructural evolution is dependent on the initial particle size and shape. As the size of particles decreases, the surface area incorporated in deformation increases. In addition, irregular particles undergo not only intended surface deformation, but also bending deformation at the bridges joining particles. Because HRNP has particles that are both small and irregular, the result is high deformation and consequential high dislocation density.
- (4) Mechanical properties of the compacted bulks are explained by crystallite size, as evaluated using the XRD line profile analysis. This indicates that the crystallite boundary acts as a main barrier to the

movement of dislocations. Therefore, the greatest strength was exhibited by HRNP, which had the smallest crystallite size among the compacts. On the other hand, other microstructural factors, total dislocation densities and grain size based on high-angle grain boundaries, could be related to compaction behaviors.

Acknowledgements This work was supported by the National Research Foundation of Korea (NRF) Grant funded by the Korea government (MSIP) (No. 2014R1A2A1A10051322).

Compliance with ethical standards

Conflict of interest The authors declare that they have no conflicts of interest.

References

- Meyers MA, Mishra A, Benson DJ (2006) Mechanical properties of nanocrystalline materials. *Prog Mater Sci* 51(4):427–556
- Viswanathan V, Laha T, Balani K, Agarwal A, Seal S (2006) Challenges and advances in nanocomposite processing techniques. *Mater Sci Eng, R* 54(5):121–285
- Koch CC (2007) Structural nanocrystalline materials: an overview. *J Mater Sci* 42(5):1403–1414. doi:10.1007/s10853-006-0609-3
- Vinogradov A (2007) Fatigue limit and crack growth in ultra-fine grain metals produced by severe plastic deformation. *J Mater Sci* 42(5):1797–1808. doi:10.1007/s10853-006-0973-z
- Lesuer D, Syn C, Sherby O (2010) Nano-scale strengthening from grains, subgrains, and particles in Fe-based alloys. *J Mater Sci* 45(17):4889–4894. doi:10.1007/s10853-010-4391-x
- Valiev RZ, Langdon TG (2006) Principles of equal-channel angular pressing as a processing tool for grain refinement. *Prog Mater Sci* 51(7):881–981
- Valiev RZ, Islamgaliev RK, Alexandrov IV (2000) Bulk nanostructured materials from severe plastic deformation. *Prog Mater Sci* 45(2):103–189
- Saito Y, Utsunomiya H, Tsuji N, Sakai T (1999) Novel ultra-high straining process for bulk materials—development of the accumulative roll-bonding (ARB) process. *Acta Mater* 47(2):579–583
- Lim C-Y, Han S-Z, Lee S-H (2006) Formation of nano-sized grains in Cu and Cu–Fe–P alloys by accumulative roll bonding process. *Met Mater Int* 12(3):225–230. doi:10.1007/bf03027535
- Valiev R (2007) The new trends in fabrication of bulk nanostructured materials by SPD processing. *J Mater Sci* 42(5):1483–1490. doi:10.1007/s10853-006-1281-3
- Kim HS, Joo S-H, Jeong H (2014) Plastic deformation and computer simulations of equal channel angular pressing. *Korean J Met Mater* 2:87–99. doi:10.3365/KJMM.2014.52.2.87
- Song Y, Wang W, Lee DJ, Jeong HJ, Lee S, Kim HS (2015) Thickness inhomogeneity in hardness and microstructure of copper after the compressive stage in high-pressure torsion. *Met Mater Int* 21(1):7–13
- Cheng S, Ma E, Wang YM, Kecskes LJ, Youssef KM, Koch CC, Trociewitz UP, Han K (2005) Tensile properties of in situ consolidated nanocrystalline Cu. *Acta Mater* 53(5):1521–1533
- Khan AS, Zhang H, Takacs L (2000) Mechanical response and modeling of fully compacted nanocrystalline iron and copper. *Int J Plast* 16(12):1459–1476
- Sciti D, Vicens J, Bellosi A (2002) Microstructure and properties of alumina–SiC nanocomposites prepared from ultrafine powders. *J Mater Sci* 37(17):3747–3758. doi:10.1023/A:101657728915
- Kang HS, Shon IJ (2014) Rapid sintering of nanostructured (Mo, W)Si₂ and its mechanical properties. *Korean J Met Mater* 8:623–629. doi:10.3365/KJMM.2014.52.8.623
- Kang B-R, J-k Yoon, Hong K-T, Shon I-J (2015) The mechanical properties and rapid low-temperature consolidation of nanocrystalline Cu–ZrO₂ composites by pulsed current activated heating. *Met Mater Int* 4:698–703. doi:10.1007/s12540-015-4366-1
- Kwon S-M, Park N-R, Shin J-W, Oh S-H, Kim B-S, Shon I-J (2015) Mechanical properties and sintering of nanostructured Ti–TiC composites. *Korean J Met Mater* 8:555–562. doi:10.3365/KJMM.2015.53.8.555
- Ahn D-H, Kim W, Park LJ, Kim HS (2014) Planar shock wave compaction of oxidized copper nano powders using high speed collision and its mechanical properties. *J Korean Powder Metall Inst* 21(1):39–43
- Ahn D-H, Kim W, Kang M, Park LJ, Lee S, Kim HS (2015) Plastic deformation and microstructural evolution during the shock consolidation of ultrafine copper powders. *Mater Sci Eng, A* 625:230–244
- Lee J-S, Choi J-P, Lee G-Y (2013) Consolidation of hierarchy-structured nanopowder agglomerates and its application to net-shaping nanopowder materials. *Materials* 6(9):4046–4063
- Ribárik G, Gubicza J, Ungár T (2004) Correlation between strength and microstructure of ball-milled Al–Mg alloys determined by X-ray diffraction. *Mater Sci Eng, A* 387–389:343–347. doi:10.1016/j.msea.2004.01.089
- Nye JF (1953) Some geometrical relations in dislocated crystals. *Acta Metall Mater* 1(2):153–162
- Lee DJ, Yoon EY, Lee SH, Kang SY, Kim HS (2012) Finite element analysis for compression behavior of high pressure torsion processing. *Rev Adv Mater Sci* 31:25–30
- German RM (2005) Powder metallurgy and particulate materials processing: the processes, materials, products, properties, and applications. Metal powder industries federation, Princeton
- Kim Hyoung Seop, Lee J-S (2004) A model on the densification of agglomerates of powders. *J Korean Powder Metall Inst* 11(4):301–307
- Hyun SK, Murakami K, Nakajima H (2001) Anisotropic mechanical properties of porous copper fabricated by unidirectional solidification. *Mater Sci Eng, A* 299(1):241–248
- Zhang P, Li S, Zhang Z (2011) General relationship between strength and hardness. *Mater Sci Eng, A* 529:62–73
- Gubicza J, Balogh L, Hellmig R, Estrin Y, Ungár T (2005) Dislocation structure and crystallite size in severely deformed copper by X-ray peak profile analysis. *Mater Sci Eng, A* 400:334–338
- Ribárik G, Gubicza J, Ungár T (2004) Correlation between strength and microstructure of ball-milled Al–Mg alloys determined by X-ray diffraction. *Mater Sci Eng, A* 387:343–347
- Chinh NQ, Gubicza J, Langdon TG (2007) Characteristics of face-centered cubic metals processed by equal-channel angular pressing. *J Mater Sci* 42(5):1594–1605. doi:10.1007/s10853-006-0900-3
- Merz MD, Dahlgren SD (1975) Tensile strength and work hardening of ultrafine-grained high-purity copper. *J Appl Phys* 46(8):3235–3237
- Nabarro FRN, Basinski ZS, Holt D (1964) The plasticity of pure single crystals. *Adv Phys* 13(50):193–323